https://doi.org/10.3311/PPci.44779

Periodica Polytechnica Civil Engineering, 70(2), pp. 717–729, 2026

Seismic Structural Damage Prediction Considering 3D Topographic and Basin Effects on the Distribution of Seismic Hazards: A Demonstration in Hong Kong

András Mahler[1], Milki M. Daniel[2], Bence Kató[2*]

[1] Department of Engineering Geology and Geotechnics, Faculty of Civil Engineering, Budapest University of Technology and Economics, Műegyetem rkp. 3., H-1111 Budapest, Hungary
[2] College of Civil and Transportation Engineering, Shenzhen University, 3688 Nanhai Avenue, Nanshan District, 518060 Shenzhen, Guangdong Province, China
[*] Corresponding author, e-mail: bkato@szu.edu.cn

Received: 18 May 2026, Accepted: 09 June 2026, Published online: 18 June 2026

Abstract

This study demonstrates a performance-based regional structural damage prediction methodology through a case study on the Tuen Mun-Yuen Long Basin in Hong Kong, incorporating 3D topographic, basin, and site amplification effects into fragility mapping. Regional-scale spectral element method simulations, accounting for soil nonlinearity, are conducted to quantify the spatial distribution of spectral acceleration amplifications (*SaAmp*). The 2%-in-50-years uniform hazard spectrum for Hong Kong was disaggregated to identify dominant magnitude-distance scenarios governing the fragility of short-period structures. An input ground motion was selected to match a short-period conditional mean spectrum, ensuring that the seismic hazard controls structural fragility. Two prototypical low-rise reinforced concrete frame structures were analyzed in ETABS to determine their modal properties and base shear threshold values corresponding to three structural component damage states defined in FEMA P-58-1. Structural fragility was subsequently mapped based on the probability of exceeding these damage states under 2%-in-50-years design spectral demand, spatially amplified using the regional *SaAmp* datasets. The resulting fragility maps reveal pronounced spatial variability in structural damage potential governed by local geological conditions. The prototypical three-story residential structures located above 20–30 m deep basin deposits exhibited collapse probabilities exceeding 50% due to double resonance between the soil and structure. The prototypical single-story warehouse structures remained resilient, with negligible damage probability. The study demonstrates that accounting for the seismic demands that govern structural fragility, together with spatially-distributed 3D site effects, strongly influences the expected level of structural damage. Neglecting these factors may lead to a substantial underestimation of seismic consequences.

Keywords

seismic fragility mapping, performance-based earthquake engineering, topographic effects, basin effects, regional ground-motion

1 Introduction

Urban earthquake risk mitigation increasingly relies on performance-based analysis to support accurate emergency response planning and reduce casualties. Current practice, however, largely performs regional-scale structural hazard assessments using generic ground-shaking intensity measures, such as peak ground acceleration (*PGA*), without accounting for their spatial variability arising from complex amplification mechanisms triggered by topography, basin geometry, and site effects. Moreover, regional structural seismic damage assessments remain scarce in the literature due to the complexity and computational cost of simulating fully coupled seismic soil-structure interaction at the scale of entire city blocks. Existing regional studies [1–3] typically provide deterministic results or conduct collapse-based assessments, which limits generalizability and does not provide a probabilistic characterization of structural safety. Recent trends in regional seismic hazard assessment and early earthquake warning systems (EEWS) have been moving toward evaluating structural damage potential using engineering-based, practical damage indicators (e.g., critical component fragility) with fully quantified uncertainties, to enable clearer risk communication and more informed decision-making.

Cite this article as: Mahler, A., Daniel, M. M., Kató, B. "Seismic Structural Damage Prediction Considering 3D Topographic and Basin Effects on the Distribution of Seismic Hazards: A Demonstration in Hong Kong", Periodica Polytechnica Civil Engineering, 70(2), pp. 717–729, 2026. https://doi.org/10.3311/PPci.44779

Despite advances in numerical simulation of regional ground motions, significant challenges remain in forecasting structural damage at this scale. Two primary limitations arise from the complexity of the model and the computational demands. First, capturing the 3D variability of ground motions induced by local site conditions and topography remains challenging [4, 5]. Second, integrating detailed structural models with regional geological models, while preserving modelling accuracy and numerical stability, remains computationally prohibitive [5]. Large urban regions may contain hundreds or thousands of distinct sites, each characterized by different soil depths, layering, topography, structural types, and structural dynamic properties.

Concerning ground motion characterization, simplified Ground Motion Models (GMMs) are most commonly used [6, 7], which typically rely on a single site parameter (e.g., V_{s30}) to scale a uniform hazard spectrum (UHS). This overly simplified approach, however, neglects key physical mechanisms governing amplification. In particular, GMM-based hazard spectra often fail to capture the effects of complex soil layering, basin geometry, and local site resonance, which strongly influence both the amplitude and frequency content of spectral accelerations (*Sa*). Amongst many researchers, Bantis et al. [8] noted that soft soils can significantly modify ground motions such as *PGA*, *Sa*, frequency content (spectral shape), amplification at specific frequencies (local resonances), and shaking duration. 3D spectral element method (SEM) simulations have demonstrated that realistic representations of topography and subsurface structure can produce substantial localized amplification. As shown by Kato and Wang [3, 5] in coastal and hilly regions, such as Hong Kong, strong impedance contrasts, variable soil thickness, and steep topography give rise to pronounced 3D site response effects. Du [9] reported amplification factors exceeding 10 at certain frequencies when modelling realistic mountainous terrain and soil layering in Hong Kong. Chen et al. [10] further showed that irregular valley and ridge geometries can produce up to two-fold differences in shaking intensity, with strongly frequency-dependent amplification patterns. Sedimentary basins similarly exert a significant influence on ground motion and structural demand. Seismic waves entering deep basin deposits may become trapped and reverberate, amplifying motion at periods corresponding to basin resonance. Amongst many others, Somala et al. [11] noted that deep sedimentary basin effects increase the consequences of earthquakes on civil infrastructure, particularly for long-period structures such as high-rise buildings and bridges. They demonstrated that the collapse fragility of tall bridges is significantly underestimated by standard models (e.g., FEMA's HAZUS) when deep-basin amplification is neglected. Parla et al. [12] showed that basin geometry, including depth, width, and impedance contrast, substantially affects fragility estimates for structures with long natural periods. Importantly, Kato and Wang [5] identified strong 3D effects even in shallow basins (<50 m), showing that bowl-shaped and half-pipe basin geometries can amplify the first three site periods (defined per 1D representative soil column) by up to five-fold at the basin center and three-fold at the edges. Overall, these findings demonstrate that ground motion amplification is highly spatially variable and strongly frequency-dependent, and therefore cannot be neglected in urban-scale hazard assessment. Without explicitly accounting for basin and topographic effects, regional ground motion estimates, and the resulting structural demand predictions, may be significantly underestimated.

To translate ground motions into predicted structural damage, performance-based engineering employs fragility curves that relate the probability of exceeding damage states to an intensity measure. In seismic risk assessment, fragility curves (e.g., as codified in FEMA P-58-1 [6]) provide the fundamental link between ground motion and building damage. However, the level of detail in fragility models varies. Camayang et al. [13] reviewed fragility methodologies and emphasized that building-specific structural capacities combined with site-specific ground motions yield the highest precision, while generic fragility functions, based on simplified ground motion parameters and structural capacity, are faster to generate but may misrepresent both the spatial distribution and magnitude of expected damage. The importance of building-specific fragility assessment has been further demonstrated for RC frame-tube tall buildings, where explicitly incorporating soil-structure interaction was shown to significantly alter fragility estimates across all damage states [14]. In regional studies, generic curves are often adopted for practicality, but this comes at the cost of reduced accuracy in representing the true vulnerability of individual structures under realistic site conditions. Accurately capturing building-specific capacities requires detailed numerical simulations of structural dynamics to define reliable damage thresholds, such as Damage States (DS) per FEMA P-58-1 [6]. Similarly, generating realistic ground motion hazards through numerical simulation requires careful selection of earthquake scenarios that are relevant to the dynamic properties (e.g., fundamental period) of the structures of interest. This selection depends on rigorous hazard disaggregation for the region, which is used to identify dominant magnitude-distance pairs (i.e., faults or seismic zones) contributing to hazard at a given structural period. Sousa et al. [15] showed that approximations in hazard disaggregation can significantly bias damage estimates. They concluded that only fault zone-by-fault zone disaggregation yields sufficiently accurate fragility results. Therefore, robust structural damage prediction requires disaggregation of the targeted hazard (e.g., 2% UHS) and subsequent generation of conditional mean spectra (CMS), conditioned around the predominant periods of the structures of interest, to select representative earthquake scenarios as input for regional-scale ground motion simulations. Any comprehensive damage prediction framework must incorporate structural hazard-consistent ground motions, site and topographic amplification effects, and accurate structural capacity models.

High-fidelity site effects and structural capacity are also central to the concept of live performance-based structural damage mapping for EEWS. In principle, such systems would rapidly estimate structural demands (e.g., floor accelerations or base shear) and associated damage probabilities for vulnerable buildings once early *PGA* estimates are available following event detection. Previous studies have explored this concept by extending performance-based approaches into the early-warning context (e.g., integrating ShakeAlert outputs with simplified structural models) [16, 17]. However, practical limitations remain. Ghahari et al. [17] note that many studies rely on highly simplified structural representations (e.g., Timoshenko beam models) to approximate multistory behavior and that these beam models introduce modelling errors that are not quantified within current FEMA P-58-1 report [6]. While, approaches that adopt high-fidelity structural capacity estimates, such as Pappin et al. [18], often neglect site effects on *PGA*. Moreover, codified homogeneous *Sa* amplification factors are not applicable to EEWS-derived estimates as the estimates are of a deterministic case and their spectral content will significantly differ from UHS-consistent *Sa*, defined by seismic codes (e.g., EC-8 [7]). In summary, current EEWS frameworks generally lack the spatial resolution and site specificity needed to predict where structural damage will concentrate. They also do not adequately incorporate accurate structural capacity models for the diverse building inventory present in urban environments.

Overall clear gap can be identified in the above discussed fields: no existing framework fully integrates 3D site amplification, disaggregation and conditional spectra to generate structure-relevant hazard, high-fidelity structural capacity data, and performance-based fragility into regional structural damage-mapping. Conventional seismic risk analyses either use uniform-hazard spectra and generic amplification factors that ignore small-scale site and regional-scale topographic effects, resulting in homogeneous structural demand on a regional or city-block scale. Likewise, EEWS typically stop at predicting shaking intensity, without mapping its implications for structural damage states regionally. There is a need for a comprehensive approach that translates a given ground motion estimate (e.g., *PGA*) into spatially varying structural damage probabilities, accounting for local geology and building properties.

Therefore, this study presents a regional structural damage-mapping approach through a case study, that combines regional 3D ground motion simulation data and high-fidelity structural capacity curves to rapidly generate regional-scale, spatially-distributed structural fragility maps, based on FEMA P-58-1 [6] critical structural component damage states. The resulting damage forecast maps in response to a given *PGA* (e.g., one predicted by an EEWS) display computed damage probabilities in a spatially explicit way, to inform seismic emergency response planning and performance-based warning thresholds for EEWS.

2 Methods

2.1 Overview

First, hazard disaggregation of a target uniform hazard spectrum (UHS) is performed to identify the earthquake source (magnitude, M_w) and path parameters (distance, R) governing the structural fundamental periods of interest. Input motions are then selected and scaled to match the conditional mean spectrum (CMS) conditioned on the chosen structural period. These motions are subsequently used in 3D spectral element method (SEM) simulations of the target region to quantify the spatially varying amplification of spectral accelerations (*SaAmp*), inherently capturing topographic, basin, and soil nonlinearity effects. Given the availability of *SaAmp* and structural capacity data, the following four-step workflow, illustrated in Fig. 1, is used to generate spatially distributed structural damage probability maps:

1. Generate the EC-8 [7] design spectral demand ($Sa(T)_d$) on rock, based on a given *PGA* demand;
2. Identify the appropriate regional spectral acceleration amplification ($SaAmp(T)$) datasets at the natural periods

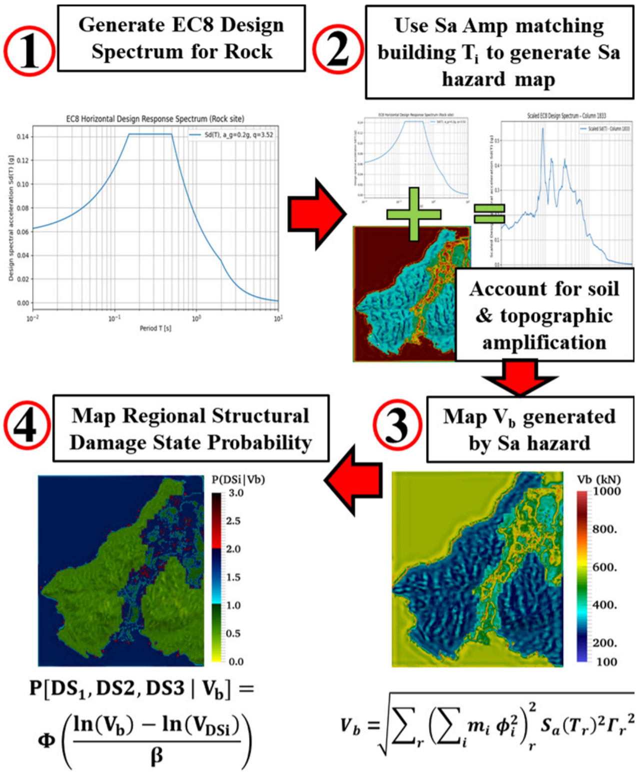

Fig. 1 Workflow of the proposed methodology

of the structure of interest and map spatially distributed spectral accelerations: $Sa(T) = Sa(T)_d \cdot SaAmp(T)$;

3. Calculate and map the expected base shear demand (V_b) for the structure of interest;
4. Calculate and map the probability of critical structural components exceeding FEMA P-58-1 [6] damage states (DS_i) per the expected base shear.

The adopted hybrid methodology combines EC-8 spectra for seismic demand characterization with the FEMA P-58-1 [6] framework for performance-based damage assessment. This approach is appropriate for Hong Kong, whose seismicity is more comparable to low-seismicity European regions reflected in the EC-8 spectral shape, while FEMA P-58-1 [6] provides a rigorous fragility-based assessment methodology. Consistency is maintained by calibrating the ground-motion dispersion parameter (β_{gm}) given in FEMA P-58-1 [6] using Hong Kong-specific probabilistic seismic hazard analysis, thereby ensuring that local seismic variability is appropriately represented by the resulting fragility curves.

2.2 Regional ground motion simulation

First, a UHS level is identified, such as a 2%-in-50-year. The UHS is then disaggregated to determine the dominant magnitude-distance pairs (i.e., faults or seismic zones) contributing to the hazard at a given structural period, T. The selected period should be representative of the range of modal periods of structures cumulatively mobilizing at least 75% of their total mass (often the median of the first flexural mode). Consequently, a single representative period can be used for a broad class of structures with similar fundamental periods, T_0. Fig. 2 (a) presents the fault zone-by-fault zone disaggregation results of earthquake magnitude-distance distributions and their respective contributions to the 2% UHS at the representative structural period of $T = 0.1$ s for Hong Kong [18]. A conditional mean spectrum (CMS) is subsequently generated, conditioned on the UHS at the representative structural period. Example CMS generated following [19, 20] are shown in Fig. 2 (b).

Given the range of controlling magnitude-distance pairs, the "Design Ground Motion Library" tool [21] is used to select and scale earthquake records that best match the CMS. The selection is evaluated using the mean squared error (MSE) of the geometric mean of the two horizontal component spectra. Ground motion selected in this manner, when used as input motion for SEM simulations ensures that the resulting hazards (e.g., *Sa* and *SaAmp*) govern the fragility of structures with predominant periods near the chosen representative period, *T*.

The selected earthquake records are subsequently applied as vertically propagating waves from the bedrock in a regional-scale SEM model. Surface topography is generated from publicly available digital elevation model (DEM) data, whereas subsurface soil and rock stratigraphy, together with their material properties, are defined using dense borehole data across the region. The model building procedure is described in detail in Kato and Wang [5]. Ground motions are simulated using the open-source SEM code SPEED [22], adopted herein for its capability to handle discontinuous (non-conforming) meshes. Defining a discontinuous interface between soft

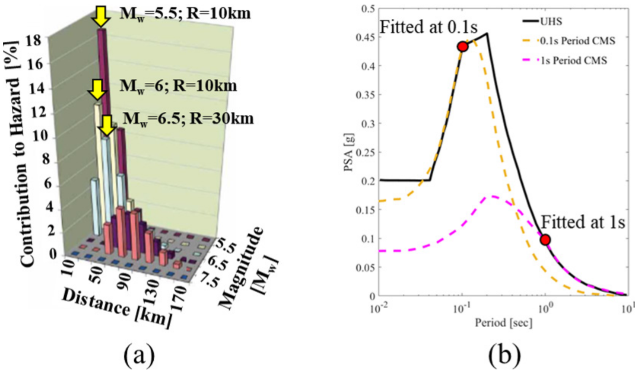

Fig. 2 Hazard identification: (a) Disaggregation of UHS at 0.1 s; (b) Examples of CMS

soil and hard bedrock layers enables independent meshing of these materials. Soil basins can therefore be discretized with fine meshes to capture high-frequency wave propagation in low shear wave velocity (V_s) materials, while larger mesh sizes are used for hard bedrock with high V_s. This approach minimizes the total number of DOFs and reduces computational cost. The shear stress-dependent nonlinear degradation of soil shear modulus (and consequently V_s), together with the increase in damping ratio, is modelled using a simplified variation of the equivalent linear approach first introduced by Seed and Idriss [23]. In the adopted formulation, the soil shear modulus, G, and damping ratio, ξ, are updated according to the experienced maximum shear stress in each soil element every time step. The major limitations of this model are that it cannot distinguish between loading and unloading and cannot capture residual behavior, i.e., the elastic stiffness and damping values are regained at the end of loading. The anelastic attenuation in SPEED [22] is implemented such that all frequencies experience the same attenuation rate per unit time. However, because a high-frequency wave completes more cycles in the same time, the attenuation per cycle is indeed smaller for high frequencies than for low frequencies. To combat this, in SPEED ξ at frequency f is proportional to a reference ξ_0 at a reference frequency f_0 ($\xi = \xi_0(f/f_0)$), where ξ_0 and f_0 are inputted according to the frequency range of the propagated wave. In this study, f_0 is chosen as the CMS conditioning period for input motion selection (10 Hz), to ensure that frequencies around the natural period of the structures of interest as well as around the peak frequency of the input motion (where overwhelming majority of seismic energy will lie) are damped correctly. Conventional G and ξ versus shear strain curves were used as material input parameters, such as Seed et al. [24] for sands and Vucetic and Dobry [25] for clays.

Accelerations are recorded across the surface of the regional model, and the corresponding 5%-damped pseudo-spectral accelerations (Sa) are computed. The calculated Sa at each surface grid point is then normalized by the bedrock outcrop free-field Sa obtained from 1D wave propagation analysis. The resulting ratio defines the mapped spectral acceleration amplification factors (*SaAmp*) relative to a free-field rock site. By explicitly modelling surface and subsurface geometry, soil layering, and material nonlinearity, the calculated *SaAmp* inherently capture the effects of local topography, basin geometry, and soil stratification. Furthermore, by selecting input ground motions determined *via* UHS disaggregation for a selected representative structural period, T, the resulting *SaAmp* are representative of earthquake scenarios with magnitude-distance pairs within the identified range (see Fig. 2 (a) yellow arrows) and directly applicable to structures with fundamental periods close to the representative period. A database of spatially mapped amplification functions, *SaAmp*(T), generated in this manner can be used to scale rock outcrop design spectra in any subsequent analyses of structures whose fundamental periods are consistent with the CMS conditioning period within the investigated region.

2.3 Calculation of structural capacity and damage states

Performance-based structural damage prediction following FEMA P-58-1 [6] employs fragility curves relating the probability of exceeding damage states (DS_i) to an earthquake intensity measure, $Sa(T)$. FEMA P-58-1 [6] provides threshold capacity values for critical structural components under seismic loading for different structural systems. For reinforced concrete (RC) frame systems, threshold interstory drift ratio (*IDR*) values are defined for three column damage states: DS_1 – minor damage, DS_2 – moderate damage, and DS_3 – severe damage. However, accurate calculation of *IDR* from $Sa(T)$ is not possible as only empirical estimates are available. In contrast, the base shear (V_b) generated by given $Sa(T)$ can be calculated analytically when the detailed dynamic properties of the structure are known, *via*:

$$V_b = \sqrt{\sum_r \left(\sum_i m_i \phi_i^2\right)_r^2 Sa\left(T_r\right)^2 \Gamma_r^2}, \tag{1}$$

where m_i is the lumped mass and ϕ_i is the modal shape amplitude at floor i for mode r of the building. $Sa(T_r)$ and Γ_r are the spectral acceleration demand and modal participation factor at the rth modal period of the building, respectively.

To accurately determine m_i, ϕ_i, and Γ_r, a high-fidelity modal analysis must be performed for each building of interest. In addition, pushover analysis is required to translate the FEMA P-58-1 [6] *IDR*-based DS_i thresholds into corresponding V_b values that produce the exact *IDR* thresholds for each DS_i. ETABS is adopted herein to conduct these structural analyses. It provides FEMA 356 report [26] compliant nonlinear hinges for modelling RC columns, beams, masonry infill walls, and their connections, together with a straightforward framework for modal and multi-modal pushover analyses. After determining the modal parameters of a structure, the relevant modes are selected to form the load patterns used in multi-modal pushover analysis. For unidirectional pushover analysis, flexural modes cumulatively mobilizing at least 95% of the total structural mass are selected to define the modal force patterns. First, the yield base shear (V_y) is extracted from the base shear-displacement curve using the idealized bilinear procedure defined in FEMA 356 report [26]. Second, the V_b – max(IDR) relationship is obtained, and the base shear values corresponding to the exact threshold IDR values for each DS_i are identified. These define the threshold base shears $\left(V_{DS_i}\right)$.

2.4 Structural fragility and damage probability mapping

Following FEMA P-58-1 [6] for seismic performance assessment, Eq. (2) is used to construct structural fragility curves and calculate the probability of exceeding a given damage state, DS_i:

$$P\left[DS_i \mid V_b\right] = \phi\left(\frac{\ln\left(V_b\right) - \ln\left(V_{DS_i}\right)}{\beta}\right), \tag{2}$$

where DS_i are damage states of the primary structural component of a building ($i = 1\ldots3$), associated with V_{DS1}, V_{DS2}, V_{DS3}, respectively. V_b is the base shear demand calculated using Eq. (1), ϕ is the standard normal distribution function, while β is the total fragility dispersion defined by Eq. (3):

$$\beta = \sqrt{\beta_{gm}^2 + \beta_{Vb}^2 + \beta_m^2}. \tag{3}$$

The total dispersion, β, arises from three sources of uncertainty:

- β_{gm} represents the uncertainty in ground motions, herein, corresponding to the uncertainty in the PGA estimate from which the EC-8 $Sa(T)_d$ design spectrum is derived.
- β_{Vb} describes the influence of record-to-record variability of the input motions used in the SEM simulations. Specifically, it accounts for how different earthquake records fitted to the same CMS affect *SaAmp* and, consequently, the calculated V_b demand.
- β_m represents the epistemic uncertainty associated with numerical and analytical models.

β_{gm} is taken as the dispersion associated with the ground motion prediction equation used to estimate PGA, whereas β_{Vb} and β_m are defined as functions of S (see Eq. (4)) and T_0 in FEMA P-58-1 [6].

$$S = \frac{Sa\left(T_0\right)W_0}{V_y}, \tag{4}$$

where T_0 is the fundamental period of the structure, V_y is the yield base shear, and W_0 is the fundamental mode seismic weight (participating mass at T_0 × 9.81 m/s^2), taken as not less than 80% of the total weight of the building.

With all parameters defined, workflow steps 1–4 are implemented as follows:

1. Following EC-8, the 5%-damped design spectral demand, $Sa(T)_d$, on a rock outcrop is generated using the PGA estimate for a target hazard level (e.g., 2% probability of exceedance in 50 years).
2. The $SaAmp(T)$ values at each grid point of the regional map are used to scale $Sa(T)_d$, producing spatially distributed $Sa(T)$ demands that account for topographic, basin, and site effects.
3. V_b is calculated at each grid point using Eq. (1), based on $Sa(T)$ and the modal parameters of the building of interest.
4. Using the calculated V_b values and the threshold base shears V_{DS_i}, the probability of exceeding each DS_i is determined using Eq. (2). If $P[DS_i \mid V_b] > 0.5$ then $P[DS_i + 1 \mid V_b]$ is recalculated iteratively until $P[DS_i \mid V_b] < 0.5$ or DS_3 is reached. The resulting fragility maps therefore display both the expected DS_i level and its exceedance probability for the considered building type.

3 Case study

3.1 Overview of the study site and structures

To demonstrate the proposed methodology, a case study was conducted for the Tuen Mun-Yuen Long district of Hong Kong (Fig. 3). The district is dominated by three prototypical building types: high-rise residential buildings with shear wall systems, three-story village houses with RC frame systems and masonry infill, and single-story warehouse structures with RC portal frame systems. As the village house and warehouse prototypes have natural periods within a similar range (~0.35–0.05 s), they were selected to demonstrate the proposed structural damage probability mapping methodology. A uniform hazard level corresponding to a 2% probability of exceedance in 50 years (2%-in-50-years UHS) was selected to calculate the regional $SaAmp(T)$ distribution, as this is the only hazard level expected to produce significant structural damage in the moderately seismic environment of Hong Kong [18]. The UHS was disaggregated to identify the magnitude-distance pairs out of 20 source zones that contribute to structural hazard in the short-period range, specifically at T = 0.1 s. Finally, an earthquake record matching the CMS conditioned on the 0.1 s ordinate of the 2%-in-50-years UHS was selected for the regional-scale ground motion simulations to quantify *SaAmp*(*T*) distributions and generate fragility maps for the village house and warehouse prototypes under a 2%-in-50-years *PGA*.

3.2 Regional ground motion simulation

The testbed for this study is the Tuen Mun-Yuen Long Paleozoic sedimentary basin in north-western Hong Kong, surrounded by Mesozoic granitic and volcanic mountains, as shown in Fig. 3. A 14 × 16 km SEM model was constructed for SPEED [22] simulations. Surface topography was generated from DEM data, while basin soil stratigraphy was defined using over 550 borehole logs provided by the Geotechnical Engineering Office of the Hong Kong government. A discontinuous interface was introduced in SPEED between the bedrock (mountain and seabed) and basin sub-domains to simplify the meshing procedure, as illustrated in Fig. 3. The basin generally consists of four soil layers with highly spatially variable thicknesses. Overlying the granite bedrock are highly decomposed, then completely decomposed volcanic rock layers, followed by a silty sand layer, and finally a Quaternary superficial deposit or reclamation fill composed of silty/clayey sand. The *Vs* values of each layer (Fig. 3) were estimated using SPT-N blow count correlations developed for the region [27]. Additional details regarding the model configuration and simulation parameters are provided in Kato and Wang [5] and are omitted here for brevity.

The 2%-in-50-years UHS for Hong Kong was disaggregated at T = 0.1 s (see Fig. 2 (a)), resulting in controlling magnitude-distance pairs within the ranges $M_w \in [5.5, 6.5]$ and $R \in [10 \text{ km}, 50 \text{ km}]$. Based on these ranges, a scaled earthquake record matching the 0.1 s CMS was selected using the "Design Ground Motion Library" tool [21]. During the fitting procedure, the expected spectral ordinate at the target period (0.1 s), although not anchored, was assigned a substantially higher weight in determining the scaling factor. The same scaling factor applied to the horizontal motions was also used for the vertical component. The selected record corresponded to the scaled earthquake whose geometric mean horizontal spectra produced the lowest MSE relative to the 0.1 s CMS, while also having the shortest duration to reduce simulation time. This selection procedure is explicitly recommended in FEMA P-58-1 [6] Appendix B.4.4 and B.7. The scaled spectra and acceleration histories of the selected M_w = 6, R = 30 km earthquake event are shown in Fig. 4.

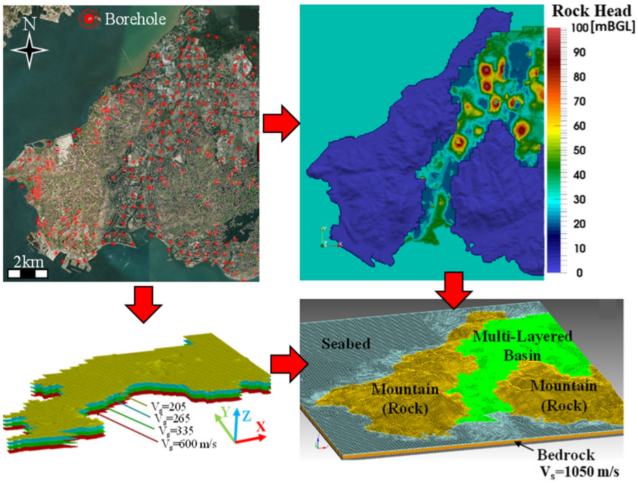

Fig. 3 Construction of the Tuen Mun-Yuen Long regional SEM model

The resulting 3D motion was applied as vertically propagating shear waves at the bottom boundary of the SEM model. Surface accelerations were recorded on an approximately 3 m × 3 m grid, and the corresponding 5%-damped pseudo-spectral accelerations, *Sa*(*T*), were computed at the same resolution. The calculated *Sa*(*T*) values were then normalized by the bedrock outcrop free-field *Sa*(*T*), producing *SaAmp* maps for $T \in [0 \text{ s}, 10 \text{ s}]$. Example *SaAmp* maps at the two orthogonal flexural fundamental periods of the selected structures are presented in Fig. 5. As the input motion was conditioned at T = 0.1 s, the resulting *SaAmp*(*T*), when applied to an EC-8 design demand spectrum, amplify or deamplify $Sa(T)_d$ around or away from the dominant periods of short-period buildings. The resulting demands therefore capture not only topographic, basin, and site effects, but also the characteristics of earthquakes governing short-period building fragility, namely events associated with the source and path parameters identified in Fig. 2 (a).

3.3 Structural analyses

The short-period structures selected for this case study were the prototypical village house and warehouse RC buildings, shown in Fig. 6, which are ubiquitous in the Tuen Mun-Yuen Long region. The single-story warehouse structure is 40 m wide (five-bay frame) and 72 m long (12 bays).

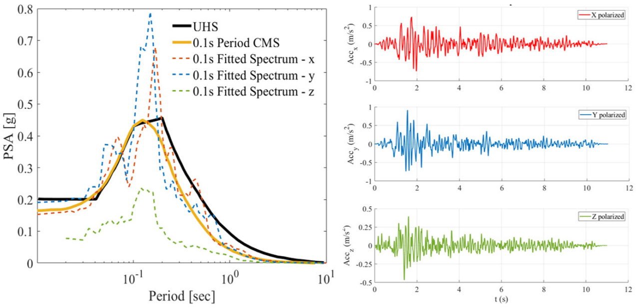

Fig. 4 CMS fitting and corresponding input acceleration time histories

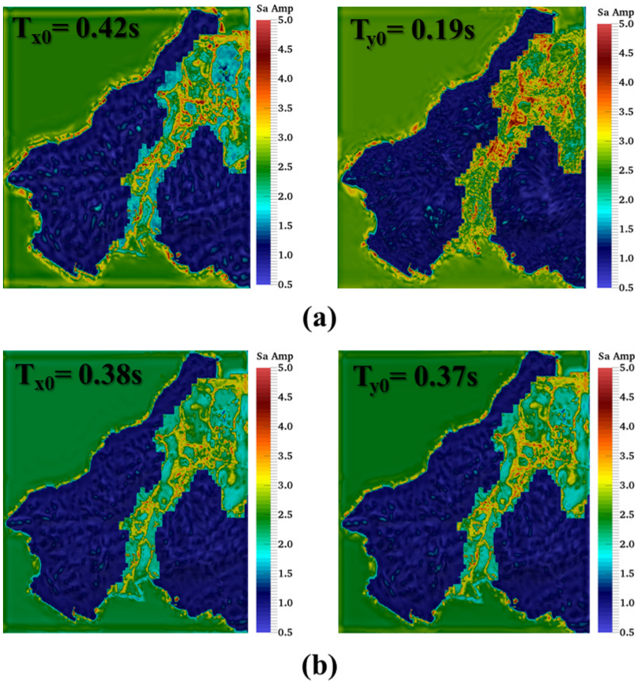

Fig. 5 Spectral acceleration amplification maps at the first period of the two example structures: (a) *SaAmp* at village house T_0; (b) *SaAmp* at warehouse T_0

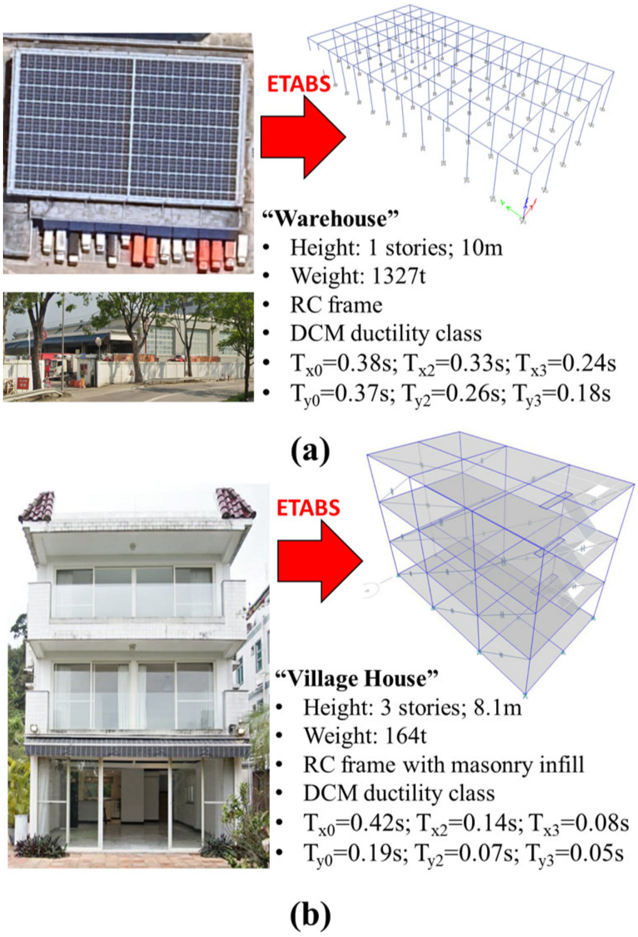

Fig. 6 The prototypical RC structures: (a) Warehouse; (b) Village house and their properties

It was modelled in ETABS as a 3D portal frame structure with RC columns measuring 0.6 m × 0.6 m, beams measuring 0.5 m × 0.6 m, and no diaphragms. C35/45 concrete and S550 reinforcement steel were assigned as material properties. The three-story village house (2.7 m per story) is 6 m wide (single bay) and 11 m long (three bays). It was modelled as a 3D portal frame structure with rigid diaphragms, and equivalent diagonal links representing masonry infill walls. The RC columns measured 0.2 m × 0.3 m, the beams 0.2 m × 0.2 m, and the diaphragms were 12 cm thick. C30/37 concrete and S220 reinforcement steel were assigned. The equivalent width of the diagonal links was calculated following FEMA 356 report [26]. Assuming a wall thickness of 15 cm, the equivalent link area, A_l, was obtained. The equivalent stiffness, k_l, and failure load, F_f, of the links were then calculated using Eqs. (5) and (6), respectively:

$$k_l = \frac{E_m A_l}{L}, \tag{5}$$

$$F_f = f'_m A_l, \tag{6}$$

where E_m = 3400 MPa is the Young's modulus of masonry in "good" condition according to FEMA 356 report [26], A_l is the equivalent link area, L is the length of the link (diagonal length of the infill wall), and f'_m = 6.2 MPa is the compressive strength of masonry prisms in "good" condition according to FEMA 356 report [26]. The total weight of each infill wall was assigned to its corresponding link for the dynamic analyses.

Nonlinearity in beams, columns, and masonry infill walls (links) was modeled using FEMA 356-prescribed [26] plastic hinges, with force-deformation relationships calibrated for each structural component. The adopted tri-linear curves correspond to the building performance levels of Collapse Prevention (CP), Life Safety (LS), and Immediate Occupancy (IO).

Since the two prototype buildings exhibit a high degree of geometric and structural symmetry, the coupled translational and torsional modes possess negligible modal participation factors and masses. Consequently, their contribution to the overall dynamic response is insignificant. Therefore, for simplicity and without significant loss of accuracy, only the modal response in the governing modal direction, corresponding to the weak structural axis, is considered in fragility assessment this case study. The weak-axis modal properties of each structure, later used to calculate the least favorable V_b demands *via* Eq. (2), are summarized in Table 1. Multi-modal pushover analyses, following the procedure described in Section 2.3, were then performed

Table 1 Weak-axis modal parameters of the example structures

Modal parameter	Village house	Warehouse
T_0 [s]	0.42	0.37
T_1 [s]	0.14	0.26
T_3 [s]	0.08	0.18
Γ_1 [–]	0.94	1
Γ_2 [–]	0.93	1
Γ_3 [–]	0.95	1
$\left(\sum_i \left(m_i \phi_i^2\right)\right)_1$ [t]	132	1314
$\left(\sum_i \left(m_i \phi_i^2\right)\right)_2$ [t]	15.4	9.8
$\left(\sum_i \left(m_i \phi_i^2\right)\right)_3$ [t]	5	0.7

to determine the yield base shear and threshold base shear values listed in Table 2. The B1041.041b component classification from FEMA P-58-1 [6], corresponding to ordinary RC moment frames with weak joints and column flexural response, was adopted for both structures to define the threshold *IDR* values associated with each DS_i.

3.4 Structural damage probability maps

To demonstrate the damage probability mapping procedure, the 2%-in-50-years hazard level (PGA = 1.95 m/s^2) from the seismic hazard analysis of Hong Kong [18] was selected as the ground motion intensity for evaluating the damage probability of the two prototypical structures ubiquitous in the Tuen Mun-Yuen Long region. In practice, the *PGA* value can be obtained directly from an EEWS to enable real-time structural damage mapping during an earthquake event.

Given PGA = 1.95 m/s^2, the design spectral demand on a rock outcrop, $Sa(T)_d$, was calculated following EC-8 (Fig. 7 black curve). The spectral demand accounting for topographic, basin, and site effects, $Sa(T)$, was then calculated at each map grid point as:

$$Sa(T) = Sa(T)_d \cdot SaAmp(T). \tag{7}$$

Table 2 Damage thresholds for the example structures

Damage parameter	Village house	Warehouse
V_y [kN]	501	7450
V_{DS1} [kN]	503	9062
V_{DS2} [kN]	532	9288
V_{DS3} [kN]	555	9503

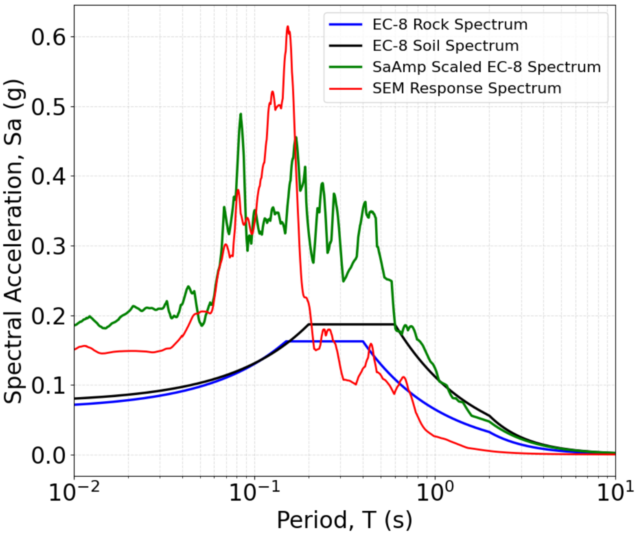

Fig. 7 Design spectra for PGA = 1.95 m/s^2 at a basin grid point, obtained using EC-8 [7] provisions, deterministic SEM simulation results, and the EC-8 [7] spectrum scaled *via* $SaAmp(T)$ derived from SEM analyses

Accounting for these effects substantially amplifies the base EC-8 demand, particularly near the representative conditioning period (0.1 s), as illustrated for an example basin grid point (Fig. 7, green curve). Fig. 7 further compares these results with the EC-8 soil Class C spectrum corresponding to local conditions (V_{s30} = 268 m/s) and the deterministic response spectrum from SEM simulation of wave propagation. The results indicate a 1.5–2× increase in short-period spectral demand when using the mapped $SaAmp(T)$ factors relative to the EC-8 soil-factors to modify the design spectrum. This discrepancy reflects the inherent limitations of simplified code-based site classification, where EC-8 soil factors (S = 1.0–1.4) represent empirical regionalized average adjustments and cannot explicitly capture basin resonance, wave focusing, or 3D site effects. In contrast, SEM simulations resolve these mechanisms directly, producing period-dependent amplifications frequently exceeding factors of 2–3 at basin focusing and resonance effect-controlled periods. Herein, this is further pronounced at short periods as $SaAmp(T)$ was derived for short-period dominant earthquake scenarios (by fitting the 0.1 s CMS), and the selected grid point is in the center of a shallow (~ 40 m) alluvial basin structure. Comparable underestimations by design code spectra of site amplification have been reported in basin environments including Mexico City [28], the Los Angeles Basin [29], Kathmandu Basin [30], and sedimentary valleys in Hong Kong [5]. Neglecting such effects may lead to unconservative seismic demand estimates and fragility predictions, particularly for structures whose fundamental periods align with amplification peaks controlled by 3D site (e.g., basin resonance) or seismic event-type (e.g., short period dominant) effects. This highlights a key limitation of uniform amplification approaches in EC-8 relative to spatially-distributed, region-specific amplification factors derived from ground motion simulations. Such an approach is also more consistent with the principles of performance-based seismic design.

Using the $Sa(T)$ data and structural modal parameters, the base shear demand, V_b, was calculated at each grid point using Eq. (1) for both the village house and warehouse structures. Herein, only fragility associated with the North-South, '*y*', directional $Sa(T)$ is considered, as they represent the highest demand (see Fig. 5). The total dispersion associated with the fragility function was then determined. β_{gm} corresponds to the weighted average standard deviation of the five attenuation relationships used in the seismic hazard analysis [18] to estimate the 2%-in-50-years *PGA* for Hong Kong, resulting in $\beta_{gm} = 0.621$. Dispersion for base shear, β_{Vb}, is not provided directly in FEMA P-58-1 [6]; however, the dispersion defined for floor acceleration, β_{aa}, was adopted as an equivalent measure because horizontal acceleration is directly proportional to the generated base shear through mass. Finally, the modelling uncertainty dispersion, β_m, is specified directly in the FEMA P-58-1 report [6]. Therefore, $\beta_{Vb} = \beta_{aa}$ and β_m were obtained from the standard according to S and T_0 (see Eq. (4)). The total dispersion for each building was then calculated using Eq. (3). Finally, given β, and V_b at each map grid point, the probabilities of exceeding the damage states, $P[DS_i \mid V_b]$, were calculated using Eq. (2).

The resulting structural damage probability maps for the village house and warehouse structures are shown in Fig. 8, with zones of high building density highlighted. For visualization purposes, a value of 1.0 was added to the calculated probability for each surpassed DS_i level. For example, $P[DS_i \mid V_b] = 1.2$ indicates a 20% probability of exceeding DS_2 and a greater than 50% probability of exceeding DS_1.

Fig. 8 (b) shows that the village house type structures can be at collapse level risk in the event of 2%-in-50-years earthquakes. The spatial pattern of high-risk zones closely follows the *SaAmp* distribution at the fundamental mode of the structure (Fig. 5 (a), T_{x0}).

This occurs because the first mode captures 85% of the participating mass and therefore dominates the structural demand. Regions with greater than 50% probability of exceeding the DS_3 (collapse state) correspond to areas where soil and structural modal responses coincide, producing double resonance. Soil depths of approximately 20–30 m in the Tuen Mun-Yuen Long region resonate with the 0.4–0.5 s period seismic waves [5], which coincides with the village house fundamental period. Consequently, spectral demands are amplified by approximately 3–5 times in these regions (Fig. 5 (a)), placing such structures at unacceptable

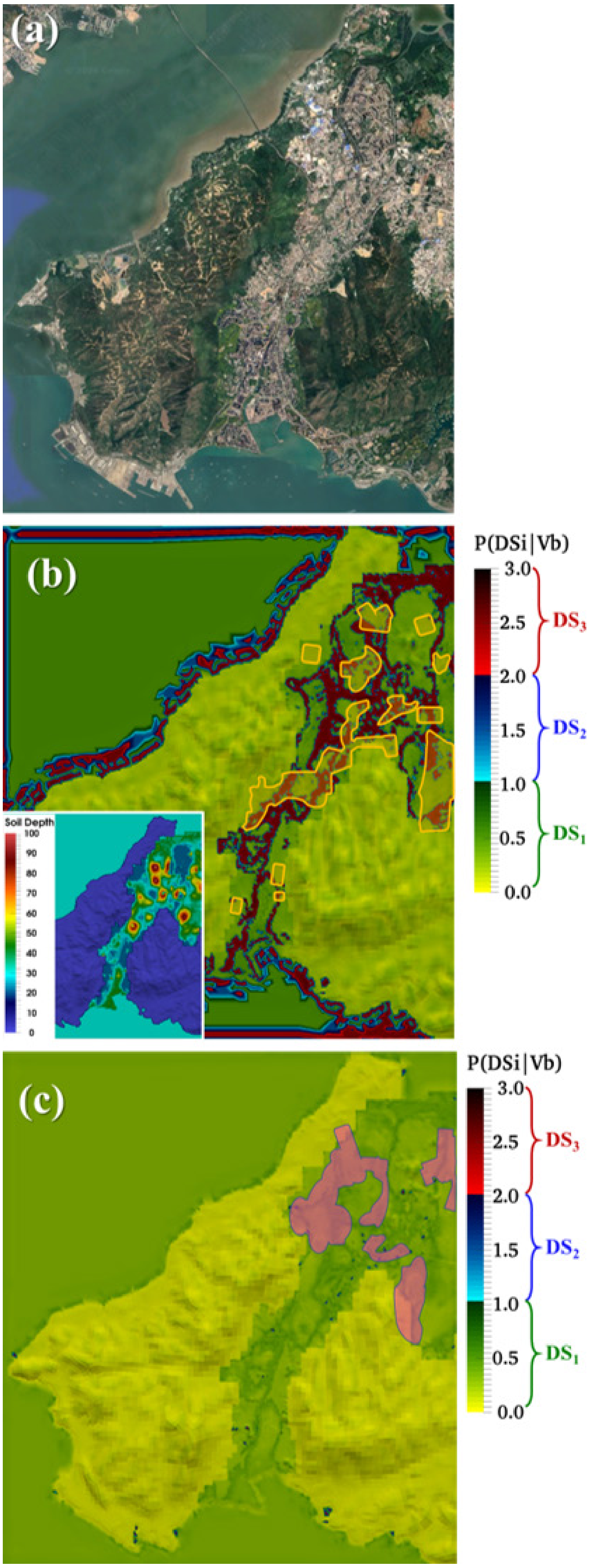

Fig. 8 Regional damage probability maps of the study region highlighting zones with high density of prototypical structures: (a) Satellite map; (b) Village house; (c) Warehouse structures

risk under the 2%-in-50-years earthquake hazard level. These results suggest that typical three-story residential buildings founded on soils of this depth are subjected to substantially increased seismic demand. Future development in regions with soil depths around 30 m should therefore incorporate rigorous seismic design considerations.

Similarly, the damage probability map for the warehouse structure (Fig. 8 (c)) shows that the highest-risk zones correlate closely with the pattern of high *SaAmp* at the fundamental mode (Fig. 5 (b), T_{y0}). However, amplification levels are lower, and the structure exhibits substantially higher V_{DS_i} thresholds (see Table 2) than the village house. Apart from several localized high-curvature hill peaks affected by topographic amplification, where significant probabilities of exceeding DS_2 are observed (blue in Fig. 8 (c)), the highest-risk zones still below 50% probability of DS_1 exceedance. This indicates that even under the highest expected seismic hazard in Hong Kong, single-story RC frame warehouses are unlikely to experience any damage.

The presented results demonstrate that considering seismic scenarios that control structural fragility, e.g., short-period dominant earthquakes when evaluating short buildings, and the accurate estimation of the spatial variability of seismic demand can strongly influence the predicted probability of structural damage at the regional scale. This effect is particularly evident in Fig. 8 (b). In most areas, where strong topographic, basin, and local site effects are limited, village houses exhibit less than 50% probability of exceeding DS_1. In contrast, in regions with strong basin effects and soil depths of 20–30 m, the same structures are likely to collapse under the same earthquake hazard level. The case study also highlights the importance of accurately quantifying structural capacity. While the prototypical three-story residential buildings exhibit high fragility, large single-story warehouse structures remain largely insensitive to earthquake damage. Overall, these observations emphasize that rigorous consideration of fragility-controlling earthquake demands, complex site effects, and accurate structural capacity assessment are essential for urban seismic resilience and performance-based design. Oversimplification or neglect of these factors may lead to severe consequences.

4 Conclusions

This study presented a FEMA P-58-1-aligned [6], performance-based methodology for regional structural damage prediction that explicitly accounts for topographic, basin, and site effects.

The framework was demonstrated through a regional case study involving two prototypical low-rise structures common in the Tuen Mun-Yuen Long region. The results indicate that under the 2%-in-50-years hazard level, moderate-magnitude earthquakes with $M_w \in [5.5,\ 6.5]$ and near-field distances $R \in [10\ \text{km},\ 50\ \text{km}]$, originating from the onshore seismic zones identified in Pappin at al. [18], generate high-frequency ground motions that pose substantial risk to low-rise residential village houses. In areas with soil depths of 20–30 m, collapse probabilities exceeding 50% were predicted. Consequently, during moderate-magnitude near-field earthquakes, gated communities and village districts in Tuen Mun-Yuen Long should be prioritized for emergency response and resource allocation. Furthermore, seismic retrofitting of existing structures and performance-based seismic design of newly constructed prototypical three-story residential buildings, incorporating the *SaAmp*(T) datasets presented herein, are recommended to improve public safety and reduce the risk of casualties.

In contrast, single-story warehouse structures are expected to withstand such earthquake scenarios with minimal or no damage. Financial losses in warehouse districts are therefore expected to remain limited, suggesting that these areas may be assigned low emergency response priority even during high-hazard earthquake events. The high seismic resilience of the warehouse structures is primarily attributable to their very low slenderness ratio (height-to-footprint area), which provides substantial lateral rigidity.

Implementation of the proposed framework is straightforward, provided that sufficiently dense borehole data are available to characterize regional subsurface stratigraphy for ground motion simulations. Because the approach relies on analytical formulations for structural demand (base shear) and closed-form fragility calculations, its computational cost is minimal. Consequently, the framework can be integrated into conventional EEWS as an additional layer for real-time regional structural damage mapping based on continuously updated *PGA* estimates. The presented results of the Hong Kong case study utilized *SaAmp*(T) datasets limited to 2%-in-50-year hazard levels and a CMS for 0.1 s. Therefore, the results are applicable only to earthquakes with *PGA* above 1.95 m/s^2 and structures with fundamental periods around 0.1 s. Furthermore, *SaAmp*(T) uncertainty stemming from possible variations in ground motions fitting a CMS were lumped into modeling dispersion as given by FEMA P-58-1 [6]. The uncertainty of *SaAmp*(T) can be quantified rigorously through linear propagation of CMS period-to-period uncertainty and will be addressed in future work. Future work will also extend the framework to coupled multi-directional fragility assessment and long-period high-rise structures, which are also prevalent in Hong Kong.

Acknowledgement

This research was supported under the Shenzhen Overseas High-Caliber Personnel Peacock Plan, 827-000947 and the Shenzhen Science and Technology Program, JCYJ20241202124408012.

References

[1] Lu, X., Tian, Y., Wang, G., Huang, D. "A numerical coupling scheme for nonlinear time history analysis of buildings on a regional scale considering site-city interaction effects", Earthquake Engineering & Structural Dynamics, 47(13), pp. 2708–2725, 2018. https://doi.org/10.1002/eqe.3108

[2] Tian, Y., Liu, S., Chen, S., Gu, D. "The site-city interaction effect uncertainty on structural responses and its application to fragility analysis of buildings in Shanghai CBD", Structures, 69, 107494, 2024. https://doi.org/10.1016/j.istruc.2024.107494

[3] Kato, B., Wang, G. "Seismic site–city interaction analysis of super-tall buildings surrounding an underground station: a case study in Hong Kong", Bulletin of Earthquake Engineering, 20(3), pp. 1431–1454, 2022. https://doi.org/10.1007/s10518-021-01295-7

[4] Chen, Z., Huang, D., Wang, G. "Large-scale ground motion simulation of the 2016 Kumamoto earthquake incorporating soil nonlinearity and topographic effects", Earthquake Engineering & Structural Dynamics, 52(4), pp. 956–978, 2023. https://doi.org/10.1002/eqe.3795

[5] Kato, B., Wang, G. "Regional seismic responses of shallow basins incorporating site-city interaction analyses on high-rise building clusters", Earthquake Engineering & Structural Dynamics, 50(1), pp. 214–236, 2021. https://doi.org/10.1002/eqe.3363

[6] FEMA "Seismic Performance Assessment of Buildings", Federal Emergency Management Agency, Washington, DC, USA, Rep. FEMA P-58-1, 2018. [online] Available at: https://femap58.atcouncil.org/documents/fema-p-58/24-fema-p-58-volume-1-methodology-second-edition/file [Accessed: 11 April 2026]

[7] CEN "EN 1998-1: Eurocode 8 - Design of Structures for Earthquake Resistance - Part 1: General Rules, Seismic Actions and Rules for Buildings", European Committee for Standardization, Brussels, Belgium, 2004. [online] Available at: https://gaprojekt.com/wp-content/uploads/2021/11/Eurocode-8-Design-of-structures-for-earthquake-resistance.pdf [Accessed: 11 April 2026]

[8] Bantis, J., Miranda, E., Heresi, P. "Simplified site response analysis for regional seismic risk assessments", Soil Dynamics and Earthquake Engineering, 188, 109022, 2025. https://doi.org/10.1016/j.soildyn.2024.109022

[9] Du, C. "Regional scale spectral element simulation of 3D topographic amplification of ground motions and associated landslide hazards", PhD Thesis, Hong Kong University of Science and Technology, 2018. https://doi.org/10.14711/thesis-991012615662503412

[10] Chen, Z.-X., Chen, G., Liu, Y. "Effects of topographic irregularity on seismic site amplification considering input signal frequency: A case study", Engineering Structures, 304, 117667, 2024. https://doi.org/10.1016/j.engstruct.2024.117667

[11] Somala, S. N., Parla, R., Mangalathu, S. "Basin effects on tall bridges in Seattle from M9 Cascadia scenarios", Engineering Structures, 260, 114252, 2022. https://doi.org/10.1016/j.engstruct.2022.114252

[12] Parla, R., Veggalam, S., Somala, S. N. "Collapse fragility of structures subjected to basin amplified ground motion: Influence of basin parameters", Advances in Structural Engineering, 29(1), pp. 78–101, 2026. https://doi.org/10.1177/13694332251348616

[13] Camayang, J. P., Dela Cruz, O., Grutas, R. "Integrating Building- and Site-Specific and Generic Fragility Curves into Seismic Risk Assessment: A PRISMA-Based Analysis of Methodologies and Applications", CivilEng, 5(4), pp. 1011–1041, 2024. https://doi.org/10.3390/civileng5040050

[14] Dorrinia, N., Pahlavan, H., Shamekhi Amiri, M., Sirjani, M. "Fragility-based Seismic Assessment of Reinforced Concrete Frame–tube Tall Buildings Incorporating Soil-structure Interaction", Periodica Polytechnica Civil Engineering, 70(1), pp. 107–122, 2026. https://doi.org/10.3311/PPci.42490

[15] Sousa, L., Marques, M., Silva, V., Varum, H. "Hazard Disaggregation and Record Selection for Fragility Analysis and Earthquake Loss Estimation", Earthquake Spectra, 33(2), pp. 529–549, 2017. https://doi.org/10.1193/062016eqs101M

[16] Zhang, H., Yu, D., Li, G., Dong, Z. "A real-time seismic damage prediction framework based on machine learning for earthquake early warning", Earthquake Engineering & Structural Dynamics, 53(2), pp. 593–621, 2024. https://doi.org/10.1002/eqe.4029

[17] Ghahari, F., Sargsyan, K., Parker, G. A., Swensen, D., Çelebi, M., Haddadi, H., Taciroglu, E. "Performance-based earthquake early warning for tall buildings", Earthquake Spectra, 40(2), pp. 1425–1451, 2024. https://doi.org/10.1177/87552930241236762

[18] Pappin, J. W., Jiang, H., Koo, R. C. H., Yu, Y. B., Kwan, J. S. H., So, M. M. L., Shiu, Y. K., Ho, K. K. S., Pun, W. K. "An updated seismic hazard analysis of the Hong Kong region", HKIE Transactions, 22(3), pp. 153–178, 2015. https://doi.org/10.1080/1023697X.2015.1061707

[19] Wang, G. "A ground motion selection and modification method capturing response spectrum characteristics and variability of scenario earthquakes", Soil Dynamics and Earthquake Engineering, 31(4), pp. 611–625, 2011. https://doi.org/10.1016/j.soildyn.2010.11.007

[20] Du, W., Ning, C.-L., Wang, G. "The effect of amplitude scaling limits on conditional spectrum-based ground motion selection", Earthquake Engineering & Structural Dynamics, 48(9), pp. 1030–1044, 2019. https://doi.org/10.1002/eqe.3173

[21] Wang, G., Youngs, R., Power, M., Li, Z. "Design Ground Motion Library: An Interactive Tool for Selecting Earthquake Ground Motions", Earthquake Spectra, 31(2), pp. 617–635, 2015. https://doi.org/10.1193/090612EQS283M

[22] Mazzieri, I., Stupazzini, M., Guidotti, R., Smerzini, C. "SPEED: Spectral Elements in Elastodynamics with Discontinuous Galerkin: A non-conforming approach for 3D multi-scale problems", International Journal for Numerical Methods in Engineering, 95(12), pp. 991–1010, 2013. https://doi.org/10.1002/nme.4532

[23] Seed, H. B., Idriss, I. M. "Influence of Soil Conditions on Ground Motions During Earthquakes", Journal of the Soil Mechanics and Foundations Division, 95(1), pp. 99–137, 1969. https://doi.org/10.1061/JSFEAQ.0001260

[24] Seed, H. B., Wong, R. T., Idriss, I. M., Tokimatsu, K. "Moduli and Damping Factors for Dynamic Analyses of Cohesionless Soils", Journal of Geotechnical Engineering, 112(11), pp. 1016–1032, 1986. https://doi.org/10.1061/(ASCE)0733-9410(1986)112:11(1016)

[25] Vucetic, M., Dobry, R. "Effect of Soil Plasticity on Cyclic Response", Journal of Geotechnical Engineering, 117(1), pp. 89–107, 1991. https://doi.org/10.1061/(ASCE)0733-9410(1991)117:1(89)

[26] FEMA "Prestandard and Commentary for the Seismic Rehabilitation of Buildings", Federal Emergency Management Agency, Washington, DC, USA, Rep. FEMA 356, 2000. [online] Available at: https://nehrpsearch.nist.gov/static/files/FEMA/PB2009105376.pdf [Accessed: 11 April 2026]

[27] Arup "Report on the Seismic Microzonation Assessment of the North-west New Territories", Geotechnical Engineering Office, Civil Engineering and Development Department, The Government of Hong Kong Special Administrative Region., Hong Kong, China, Rep. GEO Report No. 338, 2012. [online] Available at: https://www.cedd.gov.hk/filemanager/eng/content_589/er338links.pdf [Accessed: 11 April 2026]

[28] Bard, P.-Y., Campillo, M., Chávez-Garcia, F. J., Sánchez-Sesma, F. "The Mexico Earthquake of September 19, 1985—A Theoretical Investigation of Large- and Small-scale Amplification Effects in the Mexico City Valley", Earthquake Spectra, 4(3), pp. 609–633, 1988. https://doi.org/10.1193/1.1585493

[29] Wald, D. J., Graves, R. W. "The seismic response of the Los Angeles basin, California", Bulletin of the Seismological Society of America, 88(2), pp. 337–356, 1998. https://doi.org/10.1785/BSSA0880020337

[30] Trevisani, S., Pettenati, F., Paudyal, S., Sandron, D. "Mapping long-period soil resonances in the Kathmandu basin using microtremors", Environmental Earth Sciences, 80(7), 265, 2021. https://doi.org/10.1007/s12665-021-09532-7